Underestimates of Orographic Precipitation in Idealized Simulations. Part I: Evidence from Unidirectional Warm-Sector Environments

LYDIA TIERNEY[a] AND DALE DURRAN[a]

[a] *University of Washington, Seattle, Washington*

(Manuscript received 27 September 2023, in final form 4 May 2024, accepted 3 June 2024)

ABSTRACT: Heavy precipitation in midlatitude mountain ranges is largely driven by the episodic passage of weather systems. Previous studies have shown a high correlation between the integrated vapor transport (IVT) in the airstream striking a mountain and the precipitation rate. Using data collected during the Olympic Mountain Experiment (OLYMPEX) project from a pair of sounding stations and a dense precipitation network, we further document the tight relation between IVT and precipitation rate and obtain results consistent with earlier work. We also survey previous studies that simulated orographic precipitation forced by unidirectional shear flows. Some of these simulations were performed using models that produce reasonably accurate rainfall totals in nested simulations of actual events driven by large-scale flows. Nevertheless, the increase in precipitation with IVT in all the simulations with unidirectional upstream flows is far lower than what would be expected based on the observationally derived correlation between IVT and precipitation rate. As a first step toward explaining this discrepancy, we conduct idealized simulations of a midlatitude cyclone striking a north–south ridge. The relationship between IVT and rainfall rate in this "Cyc+Mtn" simulation matches that which would be expected from observations. In contrast, when the conditions upstream of the ridge in the Cyc+Mtn case were used as upstream forcing in a horizontally uniform unidirectional flow with the same IVT over the same mountain ridge, far less precipitation was produced. These idealized simulations will, therefore, be used to study the discrepancy in rainfall between simulations driven by unidirectional shear flows and observations in a companion paper.

SIGNIFICANCE STATEMENT: Idealized simulations of orographic precipitation using horizontally uniform environmental forcing fail to capture the observed relationship between integrated water vapor flux impinging on the mountain and the precipitation rate. This suggests we need to improve the design of such idealized simulations.

KEYWORDS: Mountain waves; Orographic effects; Precipitation; Cloud microphysics; Mesoscale models; Model evaluation/performance

1. Introduction

The daily weather in midlatitudes is modulated by the periodic passage of extratropical cyclones. These storm systems are of particular importance for precipitation in mountainous regions, where the majority of the annual rainfall occurs during short episodes in conjunction with strong synoptic-scale disturbances. For example, about 75% of the wintertime precipitation in the subtropical central Andes occurs during just 4–5 of the strongest annual cyclone events (Viale and Nuñez 2011). Similarly, in the Olympic Mountains, 50% of the annual precipitation was found to occur during 7–12 storms annually from 2003 to 2006 (Minder et al. 2011).

The interaction of orography with preexisting mesoscale features in midlatitude cyclones, such as fronts, rainbands, low-level blocking, and barrier jets, has been the subject of extensive previous study, as detailed, for example, in Barrett et al. (2009). Yet the bulk of the storm-averaged precipitation often falls during the passage of the warm sector when preexisting rainbands and frontal circulations are not present and when the synoptic-scale winds impinging on the orography are approximately unidirectional with height (Zagrodnik et al. 2019). Zones of enhanced water vapor flux, known as "atmospheric rivers," are often present in the warm sector. Neiman et al. (2002) found a strong correlation between maximum wind speed in the low-level jet (LLJ) within the atmospheric river and the orographic rain rate during warm-sector events with unblocked flow. Neiman et al. (2009) showed the correlation between 4 years of precipitation at a mountain site near the coast in Northern California and the oncoming winds at 1 km MSL could be improved by multiplying those winds by satellite-retrieved total column water vapor to obtain a "bulk integrated water vapor (IWV) flux." Kingsmill et al. (2016) found a strong correlation between the upslope IWV flux measured by remote sensing on the Northern California coast and precipitation observed at a downstream mountain site.

If the dynamics of orographic precipitation in the warm sector are simply produced by forced lifting as an airstream travels up the mountain slope and perhaps over a layer of blocked flow lying against the orography (Hughes et al. 2009; Lundquist et al. 2010), it is hardly surprising that there is a strong correlation between the precipitation rate and the bulk IWV flux. When sufficient data are available for its computation, even tighter correlations might be expected for the vertically integrated upslope vapor transport ($IVT_{\perp}$), in which the influence of the vertical variation in the winds on the moisture flux perpendicular to the mountain is more precisely evaluated as

$$IVT_{\perp} = \int_0^{z_t} \rho q u_{\perp}\, dz, \tag{1}$$

Corresponding author: Dale Durran, drdee@uw.edu

DOI: 10.1175/JAS-D-23-0177.1

where ρ is the density of dry air, q is the water vapor mixing ratio, $u_\perp$ is the component of the wind perpendicular to the mountain barrier, and z_t is some level above which the water vapor concentrations drop to very small values.

Most idealized numerical simulations of orographic precipitation have considered moist unidirectional shear flows impinging on a 2D or 3D mountain barrier (Colle 2004; Cannon et al. 2012; Siler and Durran 2015; Picard and Mass 2017; Purnell and Kirshbaum 2018; Kirshbaum and Schultz 2018), a configuration that might be assumed to adequately approximate quasi-unidirectional unblocked flow in the warm sector of midlatitude cyclones. As will be discussed in this paper, these idealized studies also yield a strong correlation between the precipitation rate and the $IVT_\perp$, but surprisingly, the ratio of the precipitation to the $IVT_\perp$ in these simulations is substantially lower than that obtained in observational studies of warm-sector orographic precipitation.

In section 2 of this paper, we present an analysis of the upstream $IVT_\perp$ and precipitation during the warm-sector periods of six land-falling winter storms observed during the 2015/16 Olympic Mountain Experiment (OLYMPEX) campaign in western Washington (Houze et al. 2017). We compare these values to previously published idealized simulations of horizontal unidirectional shear flows over terrain matching the Olympic Mountains. We find that the observed storms produced much more precipitation than idealized simulations with similar upstream $IVT_\perp$. In section 3, we extend the comparison between observed and idealized cases to several other previous studies, again finding substantially more precipitation occurring in observed cases than in idealized simulations with similar $IVT_\perp$.

In section 4, we describe a novel set of idealized numerical simulations designed to isolate the impact of the synoptic-scale flow on orographic precipitation. We conducted a convection-permitting simulation of an idealized midlatitude cyclone developing from an isolated PV anomaly in a zonally periodic, baroclinically unstable channel flow. The fronts associated with a mature cyclone encounter an isolated mountain ridge. A companion simulation of flow over the same 3D ridge was conducted, forced by an upstream unidirectional flow with horizontally homogeneous vertical profiles of $u_\perp$, temperature, and moisture taken upstream of the ridge within the warm sector of the simulated cyclone. The $IVT_\perp$ and terrain geometries in these "Mtn+Cyc" and "Shear" simulations are closely matched, but similar to the difference between previous observed events and simulations forced by unidirectional upstream winds, the precipitation rates are substantially higher in the Mtn+Cyc case than in the Shear simulation. The processes responsible for the difference between this pair of simulations and an additional simulation with the same cyclone passing over flat terrain are analyzed in detail in a companion paper (Tierney and Durran 2024).

2. Relation between IVT and precipitation rate during OLYMPEX in observations and idealized studies

a. IVT calculations and rain gauge network

Measuring $IVT_\perp$ and collecting representative observations of the resulting orographic precipitation is challenging. One of the best datasets for this purpose was collected during OLYMPEX, which took place from November 2015 through January 2016 on the Olympic Peninsula in Washington state. Throughout the campaign, soundings were regularly taken at two locations immediately upstream of the mountains: Quillayute Airport and Taholah (see Fig. 1 for locations). Hourly precipitation rates were collected over a network of rain gauges on the windward (southwestern) slopes and upstream of the Olympics, and radar observations were conducted with both the NASA S-band Dual Polarimetric Radar (NPOL) scanning from Taholah, Washington, and a mobile Doppler on wheels (DOW).

We identified six periods of steady precipitation from the OLYMPEX campaign during which there was little variation in the wind direction with height. To determine the timing of each event, we compared surface maps and the radiosonde data with the warm-sector periods identified in previous publications. The timing of our first five events matches warm-sector events 1–5 in Purnell and Kirshbaum (2018). For the final event, we focused on a period of long-lived precipitation between 1800 UTC 12 December 2015 and 1400 UTC 13 December 2015 that included warm-sector conditions (McMurdie et al. 2018). Although there were other cyclonic systems that produced precipitation during the OLYMPEX campaign, these six periods were selected due to the increased availability of rain gauge and radiosonde data. The dates and times of these events are listed in Table 1.

The Olympic Mountains are a quasi-circular massif, with a peak elevation of 2428 m. To characterize the precipitation over the windward slope of the terrain, we averaged the rainfall measured at the seven locations straddling the Quinault River basin shown in Fig. 1. The altitudes of these rain gauge stations ranged from 188 to 1484 m.

For comparison to idealized simulations, we chose a 110-km-long, 22-km-wide box straddling a line running from the Taholah sounding location to the highest peak. Letting this line define the x axis, the terrain within the box was averaged along a 22-km-wide segment parallel to the y axis, and a cosine curve fitted by eye to the high points in the averaged terrain. This cosine curve has a double amplitude of 1440 m (the fitted terrain height) and a quarter wavelength of 42.5 km (the half-width at half-height). This cosine is plotted in Fig. 2, along with the averaged orography and the (x, z) locations of the observing stations, where z is the height MSL. Note that all the stations are sited at local prominences exceeding the y-averaged terrain except the Enchanted Valley location.

A visual estimate of the extent to which these seven stations sample the geographic distribution of warm-sector precipitation during the 13 November, 3 December, and 8 December events is provided in Fig. 3, which is adapted from Fig. 5b of Zagrodnik et al. (2021). Figure 3 shows the distribution of precipitation rates during these events as simulated using the Weather Research and Forecasting (WRF) Model. At least for these three events, the simulated precipitation averaged over the gauge locations in the network seems likely to underestimate the actual WRF-simulated upslope-averaged rainfall. For example, although there are extensive regions on the southwestern

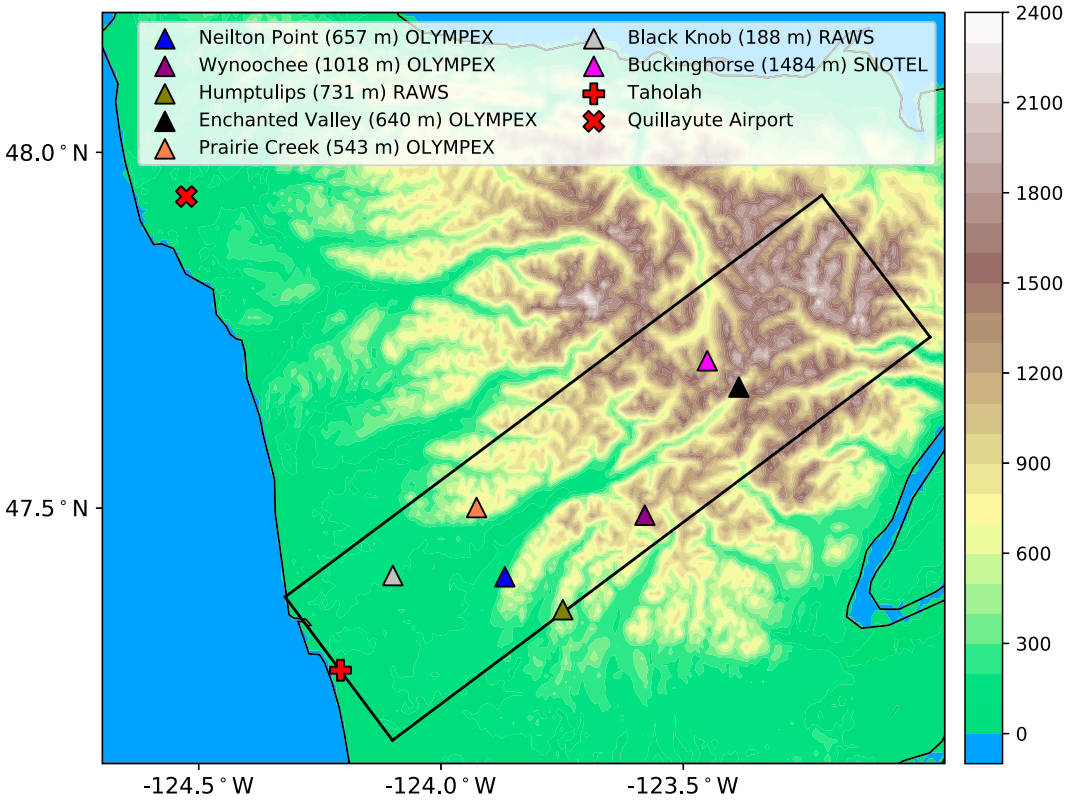

FIG. 1. Locations of the rain gauges (colored triangles) and the soundings sites at Taholah (red +) and the Quillayute Airport (red *x*). The black rectangle shows the 22-km-wide region over which the terrain is averaged perpendicular to the up-valley axis.

slopes where the simulated precipitation rate exceeds 9 mm h^{-1}, only two of the seven network sites lie in those regions. Nevertheless, we report averages from this network because it gives the best available combination of temporal and spatial coverage during the events in Table 1.

The Enchanted Valley rain gauge data were not available for the first two warm-sector events, those beginning on 13 November and 17 November. The Neilton Point gauge was also not available for the 13 November event. For all other events, data from all seven rain gauges were available. For each event in Table 1, we calculated the average hourly upslope precipitation rate by taking the mean of the hourly precipitation rate over all available gauges.

The mean upslope wind direction for our rain gauge network is directed roughly toward the northeast. The OLMPEX sounding locations are, however, very close to the foot of the mountains and may sample winds that have been partially deflected by terrain-induced blocking and diversion of the low-level flow. The precise effective upslope wind direction for the rain gauge network as a whole is also unknown. Therefore, to identify the constant wind direction onto which the full wind vector is projected in our $IVT_{\perp}$ calculations, we tested a series of possible wind directions and, independently for each station, selected the one that maximized the correlation between the IVT at each sounding location and the upslope precipitation observed over the network.

For Taholah, the optimal correlation was obtained by projecting the horizontal velocities onto the vector originating from 251°. The optimality of 251° may result from a modest deflection of flow that might have been more directly from the southwest (SW) farther upstream. The optimal correlation

TABLE 1. Dates of OLYMPEX events used in our analysis.

Event start day	Event start time (UTC)	Event end day	Event end time (UTC)
13 Nov 2015	0300	13 Nov 2015	1200
17 Nov 2015	1000	17 Nov 2015	1700
3 Dec 2015	1000	3 Dec 2015	2100
6 Dec 2015	0000	6 Dec 2015	1300
8 Dec 2015	1300	9 Dec 2015	0000
12 Dec 2015	1800	13 Dec 2015	1400

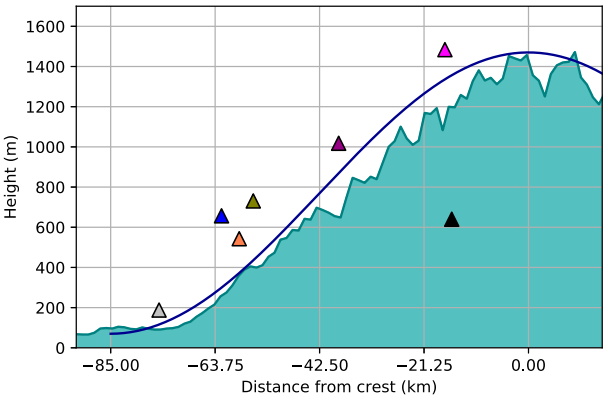

FIG. 2. Terrain as a function of x, with $x = 0$ at the approximate location of the highest orography, 92 km from Taholah: y-averaged terrain height (shading) and reference cosine curve (dark blue line). The (x, z) locations of the rain gauge stations are plotted as triangles using the same color key as in Fig. 1.

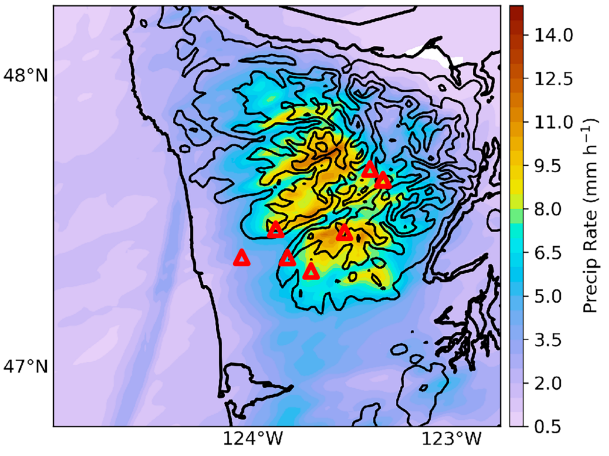

FIG. 3. Average WRF surface precipitation rate for three simulated warm-sector events adapted from Fig. 5b of Zagrodnik et al. (2021). The locations of the rain gauge stations used in our analysis are indicated with red triangles.

at Quillayute was for winds from 224°, closely aligning with flow from the southwest.

There is a short delay between the time air passes over the sounding stations and when representative portions of the same air mass pass over the rain gauge network. Based on trajectory calculations using low-level upslope winds of 15 m s^{-1}, we associated the Taholah $IVT_{\perp}$ measurements with hourly precipitation totals from the second hour following the radiosonde launch. Since locations of the Quillayute sounding and the gauge network do not lie along the same low-level air parcel trajectories during warm-sector rain events, we selected the time delay for Quillayute that gave the highest correlation between $IVT_{\perp}$ and precipitation rates over the network. Following this approach, the Quillayute $IVT_{\perp}$ measurements were associated with hourly precipitation totals from the first hour following the time of the radiosonde launch.

b. *Comparing IVT and rainfall rates*

The $IVT_{\perp}$ from each of the soundings and the hourly and spatially averaged precipitation rate over the gauge network are plotted as a function of time in Fig. 4 for multiday periods surrounding each of the events listed in Table 1. Black triangles on the time axis indicate the start and end of each event, which, in the first five cases, are the warm-sector period. Data from outside the indicated periods were not used in the subsequent analysis. Clearly, there is a correlation between $IVT_{\perp}$ and the precipitation rate, with an r^2 value of 0.87 at Quillayute and 0.82 at Taholah.

The rain rates averaged over the gauge network are plotted as a function of $IVT_{\perp}$ in Fig. 5, along with the least squares best-fit line to both the Quillayute and Taholah data, which has an r^2 value of 0.85. The slope of this line is 0.014 mm h^{-1} (kg m^{-1} $s^{-1})^{-1}$, implying that an increase of 200 kg m^{-1} s^{-1} in $IVT_{\perp}$ is associated with an increase of 2.8 mm h^{-1} in the upslope precipitation rate. Also plotted in Fig. 5 are points showing the precipitation rate as a function of IVT from two previously published idealized studies using the actual Olympic Mountains orography and representative upstream soundings. These studies used horizontally uniform upstream thermodynamic soundings with unidirectional horizontal winds.

The first of these studies (Picard and Mass 2017) examined the effect of flow direction on precipitation in the Olympic Mountains. Their steady upstream environmental conditions approximate a sounding taken at Quillayute at 1200 UTC 7 January 2009, except they specified various directions for their unidirectional upstream flow. The horizontal structure of the flow was a broad Gaussian jet with e-folding scale of 111 km that is similar to the scale of the entire Olympics massif. We compute the IVT for the core of their horizontal jet, which is meant to approximate an atmospheric river. In their Fig. 9, they report 24-h precipitation totals from their quasi-steady-state simulations in the Queets River basin for a range of wind directions. The Queets River basin is adjacent to the Quinault River valley and spans a similar range of terrain elevations roughly between 0 and 1500 m. The teal diamond in Fig. 5 shows their precipitation rate for winds from 247°, which was directly upslope and gave the maximum precipitation rate. This was also the highest precipitation rate they obtained using other flow directions (all having the same IVT) in any of the other three basins they considered. Nevertheless, as apparent in Fig. 5, the IVT required to give this precipitation rate in their simulations is more than three times higher than that which would be expected to produce the same rainfall rate using the best-fit line from the OLYMPEX observations.

The second of these studies (Purnell and Kirshbaum 2018) investigated the impact of the synoptic environment on orographic precipitation during the OLYMPEX campaign. As part of the study, they simulated the precipitation generated as a horizontally uniform flow with a prototypical OLYMPEX warm-sector sounding in which unidirectional vertically sheared horizontal winds encountered the actual Olympic Mountains orography. The product of the dying ratio (DR_w) over the windward slope times the IVT from Table 6 in Purnell and Kirshbaum (2018) gives their average orographic precipitation rate over a 40-km-wide box extending

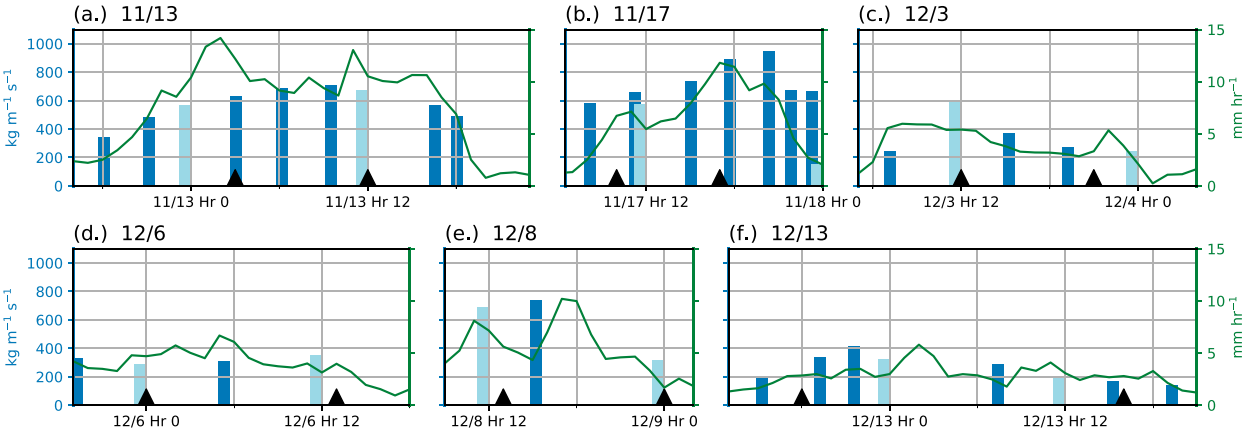

FIG. 4. IVT$_\perp$ (kg m^{-1}) from Taholah (dark blue bars) and Quillayute (light blue bars) and hourly averaged rainfall rates (mm h^{-1}) over the gauge network plotted as a function of time surrounding the six events listed in Table 1. Individual events are labeled as month/start date on each subpanel. Black triangles on the time axis mark the beginning and end of each event.

100 km upstream of the peak. Their basic warm-sector simulation, with an IVT of 607 kg m^{-1} s^{-1}, yields an area-averaged precipitation rate of 0.88 mm h^{-1} and appears plotted as the lower teal cross in Fig. 5. Once again, this is far less than would be expected for the same IVT$_\perp$ using the best-fit line from the OLYMPEX observations.

Purnell and Kirshbaum (2018) also examined the influence of the seeder–feeder mechanism on the same prototypical warm-sector flow. Ice crystals were generated aloft in their simulations by adding advective contributions to the potential temperature and moisture variables from a steady horizontally uniform ascent in the mid- and upper troposphere, which maximized at 0.2 m s^{-1}. Such an ascent was designed to roughly include the influence of synoptic-scale ascent and resulted in more than a factor-of-three increase in the windward-slope precipitation. But as apparent in Fig. 5, even with this significant seeder–feeder enhancement, the precipitation rate remains significantly below what would be expected for the same IVT$_\perp$ based on the OLYMPEX observations.[1]

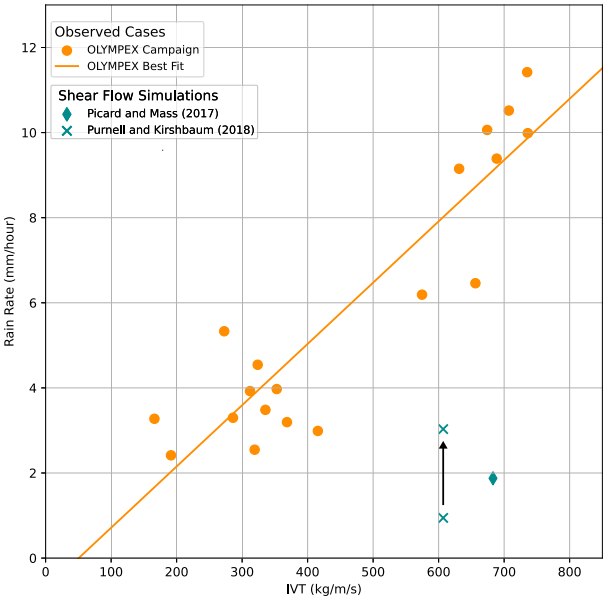

FIG. 5. Rain rates averaged over the gauge network plotted as a function of IVT$_\perp$ for the OLYMPEX events (orange dots), along with the best-fit line (orange). Rainfall rates plotted as a function of IVT estimated from previously published simulations forced by unidirectional flow using idealized OLYMPEX soundings and actual Olympic Mountains orography in teal. The arrow indicates an increase in simulated precipitation with vertical transport by uniform large-scale ascent included to trigger seeder–feeder enhancement.

The deviation of the Picard and Mass (2017) and Purnell and Kirshbaum (2018) WRF Model simulations from the observed relation between IVT$_\perp$ and rainfall rate is more striking in the context of Fig. 3, which suggests the gauge network might be distributed in a way that would underestimate the average upslope precipitation in WRF Model simulations of warm-sector events. Yet twice-daily runs of the precursor to the WRF Model, the Fifth-generation Pennsylvania State University–National Center for Atmospheric Research Mesoscale Model (MM5), accurately simulated total rainfall for the full rainy season and for the sum of the largest events for several years over this same southwest sector of the Olympic Mountains (Minder et al. 2008). As we will show, particularly in Part II of this paper (Tierney and Durran 2024), the problem is not with the model per se but rather the design of these semi-idealized simulations.

3. Beyond the Olympic Mountains

In the preceding section, we compared the relation between IVT$_\perp$ and rainfall rate observed over the Olympic Mountains

[1] Visual comparison of Fig. 7b (retrieved rainfall) and Fig. 11b (computed rainfall with seeder–feeder enhancement) in Purnell and Kirshbaum (2018) also shows underprediction on the windward slopes in the vicinity of our gauge network though perhaps by less than that in Fig. 5.

with simulations of orographic precipitation in the same region driven by unidirectional upstream flows. In this section, we expand our focus to compare the $IVT_{\perp}$–rainfall rate relationship in previously published observational studies at other locations and other idealized unidirectional flow simulations.

a. *Observational studies*

In a study spanning 10 years of cool-season data, Kingsmill et al. (2016) examined the joint distribution of the IWV flux measured at an upstream coastal station at Bodega Bay (elevation 15 m MSL) and the precipitation rate observed at Cazadero (478 m MSL) in the coastal mountains of Sonoma County, California, which have peak elevations ranging from 627 m at Buck Knoll (northeast of Cazadero) to 747 m at Centennial Mountain (farther north). They computed a best-fit line to almost 4000 hourly observations when there was nonzero upslope flow and the hourly precipitation exceeded 0.25 mm. Their data include all types of upslope precipitation events, not just warm-sector conditions, and this likely is the reason the square of their correlation coefficient is 0.45, much less than our r^2 of 0.85. Their r^2 value of 0.45 is consistent with the correlation Rutz et al. (2014) obtained studying the relation between IVT and precipitation over the western United States. Also of note is that the observations considered in this study were collected in regions where Rutz et al. (2014) found the highest correlation between IVT and precipitation.

For our purposes, the correlation between IVT and precipitation is somewhat less important than the average rate at which precipitation increases with IVT. Despite the substantial difference in topography between the Olympics and the coastal mountains, the best-fit line from Kingsmill et al. (2016), which is plotted as the brick-red dashed line in Fig. 6 (after converting their reported units of IWV flux to kg m^{-1} s^{-1}), is almost identical to the line we obtained using OLYMPEX data.

A little north of the location of the Kingsmill et al. (2016) study, Michaelis et al. (2021) analyzed two atmospheric river (AR) events that caused heavy precipitation in the Russian River watershed, which extends from sea level to elevations of about 900 m. Using data from Fig. 3 in Michaelis et al. (2021), the average IVT and areal-mean precipitation rates over each AR event are plotted as brick-red squares in Fig. 6. The point with the lowest IVT (≈285 kg m^{-1} s^{-1}) is the average for the 24–26 January 2010 event; that with the highest IVT (≈715 kg m^{-1} s^{-1}) is the average for the much stronger 10–13 December 2014 case. Also plotted with an IVT of 361 kg m^{-1} s^{-1} is the 6-h maximum IVT and precipitation rate for the 24–26 January 2010 event as listed in their Table 1. The equivalent 6-h maximum value for the 10–13 December 2014 case (IVT 1208 kg m^{-1} s^{-1} and rain rate 10.7 mm h^{-1}) is not plotted because it would lie off-scale. The Michaelis et al. (2021) data points lie roughly along a line with a shallower slope than the best linear fit of the OLYMPEX data points but give precipitation rates for a given IVT that are roughly twice that from the various idealized shear-flow simulations (teal symbols).

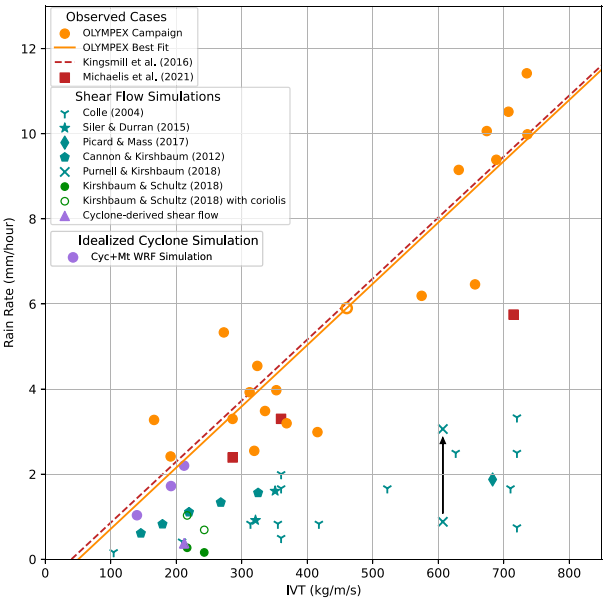

FIG. 6. As in Fig. 5, but for the addition of observational studies outside the Olympics (brick-red symbols) and shear-flow simulations of orographic precipitation over idealized terrain (teal symbols). The best-fit line for 10 years of observations in Kingsmill et al. (2016) is shown by the brick-red dashed line. Violet symbols show results from our idealized baroclinic cyclone simulation (circles) and the corresponding shear flow (triangle).

b. *Idealized shear-flow simulations*

The IVT and rainfall rate data from four additional idealized numerical simulations of orographic precipitation are also plotted in Fig. 6. Colle (2004) conducted a large number of two-dimensional simulations of airstreams with constant moist Brunt–Väisälä frequency and cross-mountain wind speed flowing over a Witch-of-Agnesi mountain profile. Only those simulations with physical parameters roughly relevant to our real storm simulation cases are plotted as the teal "*Y*" symbols in Fig. 6. The plotted simulations include cases with freezing levels between 1000 and 500 hPa, terrain half-widths at a half-height of 50 km, mountain heights between 500 and 1500 m, and upstream wind speeds ranging from 5 to 30 m s^{-1}. The procedure we used to compute the IVT and estimate a very generous upper bound on the average windward-slope precipitation in these simulations is described in the appendix. As apparent in Fig. 6, the precipitation rates generated by a given IVT in the Colle (2004) simulations are far less than that which would be expected from the observational studies.

Cannon et al. (2012) investigated the effect of embedded convection on orographic precipitation enhancement through a series of numerical 3D simulations of moist airstreams encountering barriers with a Gaussian cross-ridge profile and uniform along-ridge structure. They report the IVT in the horizontally uniform upstream environment for each of their simulations, which increased as the surface temperature varied between 277.5 and 287.5 K. The upstream wind was 15 m s^{-1} and constant with height. These upstream conditions were

"based on a six-year precipitation weighted climatology of the midlatitude mountain ranges along the West Coasts of the Americas" (Cannon et al. 2012). We computed an upper bound on the average windward-slope precipitation rates for their 1-km-high mountain simulations as detailed in the appendix. These IVT and precipitation rates are plotted as teal pentagons in Fig. 6. Although they are upper bounds, these precipitation rates are roughly half the values that would be expected for the same IVT from observations.

Siler and Durran (2015) investigated the influence of tropopause height on orographic precipitation. They conducted 3D numerical simulations of a horizontally uniform upstream flow in which winds increased with height throughout the troposphere. The 1-km high terrain was a finite-length ridge having a Witch-of-Agnesi cross-mountain profile with a half-width at half-height of $a = 25$ km. The upslope precipitation was determined by dividing the full cross-ridge-integrated precipitation rate reported in the caption of Fig. 8 of Siler and Durran (2015) by the length of the windward slope ($2a$), which once again gives an overestimate of the average windward-slope precipitation rate. The IVT was calculated from specified thermodynamic and wind speed profiles. These IVT–rainfall rate pairs are plotted as the teal stars in Fig. 6. Despite being overestimates, the precipitation rates of Siler and Durran (2015) are roughly one-third of what would be expected using the observed correlation between IVT and precipitation rate.

Kirshbaum and Schultz (2018) simulated flow over a 1.5-km-high Gaussian ridge with an e-folding scale of 50 km and along-ridge to cross-ridge aspect ratio of 3. Horizontally uniform winds increased linearly with height from 10 m s^{-1} at the surface at the rate of 0.0015 s^{-1}. When the Coriolis force was included, a constant north–south environmental temperature gradient was specified to be in thermal wind balance with the constant vertical shear. As shown in their Figs. 10b and 10e, the Coriolis force turned the incoming westerly flow to enhance the precipitation on the northern half of the ridge. We plot the average upslope precipitation rate (estimated from their Figs. 10b,e) at the north–south location of maximum intensity against the IVT upstream of the north–south centerline of the ridge as open green circles in Fig. 6. The equivalent quantities are also plotted for no-Coriolis-force ($f = 0$) simulations (from their Figs. 10a,d) as solid green circles. Comparing the solid and open circles, it is apparent that the Coriolis-force simulations generate much more intense precipitation than those with $f = 0$. Yet even with $f = 10^{-4}$ s^{-1}, the relation between IVT and precipitation rate in the region of maximum intensity on the northern portion of the ridge is no more than roughly half of that which might be expected from the best-fit lines for the Olympics or the California coastal ranges.

4. Idealized multiscale and shear-flow simulations

The preceding results suggest that idealized simulations of orographic precipitation forced by unidirectional horizontal winds substantially underestimate the rainfall rates that would be produced in real atmospheric events with the same value of IVT$_\perp$. Even the simulations in Purnell and Kirshbaum (2018) that include uniform large-scale ascent, thereby producing significant enhancement via the seeder–feeder mechanism, still gave rainfall rates less than half of what would be expected in a real-world event with the same incoming IVT. Yet as previously noted, daily predictions of orographic precipitation with similar mesoscale numerical models do give accurate climatological rainfall totals.

To better investigate the problems that arise with simulations of orographic precipitation forced by horizontally uniform upstream conditions, we conduct additional idealized numerical model simulations. We adopt a multiscale approach, simulating the development of a midlatitude cyclone in a simple baroclinically unstable channel flow on an outer 12-km mesh. We capture finer-scale features of the interaction of this system with an isolated ridge on a finer 4-km nested mesh. We extract a sounding matching the upstream conditions on the fine mesh and use this sounding to create an additional simulation on the fine mesh in which the synoptic-scale flow impinging on the ridge is unidirectional, horizontally homogeneous, and vertically sheared.

a. Simulation configurations

Our simulations were conducted using the Advanced Research version of WRF (WRF-ARW) model, version 3.8.1 (Skamarock and Klemp 2008). To generate a realistic cyclone, baroclinically unstable x-invariant initial conditions in a periodic f-plane channel are generated from prescribed y–z distributions of potential vorticity (PV) and relative humidity following the procedure in Lloveras and Durran (2024). Considerable care is required to ensure that the susceptibility of vertical motions to moist convective instability is realistic throughout the domain, which requires appropriate specification of the dry static stability, the temperature, and the moisture content. Figure 7 shows the initial baroclinic jet and potential temperature profile used in this simulation.

This initial state was chosen to roughly approximate the Northern Hemisphere January climatological values for wind, temperature, static stability, and moisture profiles (Fleming et al. 1990; Wilcox et al. 2011; Marshall and Plumb 2012). We also examined case studies to ensure that the idealized cyclone produces realistic warm and cold fronts and that soundings taken from various sectors of the storm are representative of what would be expected for a cyclone passing over land (Doyle and Bond 2001; Field and Wood 2007). Note, in particular, that our goal is to simulate a prototypical midlatitude event, not a prototypical OLYMPEX event.

The growth of the cyclone is triggered by an isolated PV perturbation of the form

$$Q'(x, y, z) = Q_0 e^{-(s/\delta_h)^2} e^{-[(z-z_c)/\delta_v]^2}, \tag{2}$$

where $s^2 = (x - x_c)^2 + (y - y_c)^2$, $Q_0 = 0.3$ PVU (1 PVU = 10^{-6} K kg^{-1} m^2 s^{-1}), $\delta_h = 500$ km, $\delta_v = 500$ m, and $(x_c, y_c, z_c) = (2280, 3120, 7.5)$ km. As in Menchaca and Durran (2017), this PV distribution is inverted assuming quasigeostrophic balance to recover the geopotential height field. The velocity and thermodynamic perturbations are then recovered from hydrostatic, geostrophic, and thermal wind balance and added to the background zonally uniform fields.

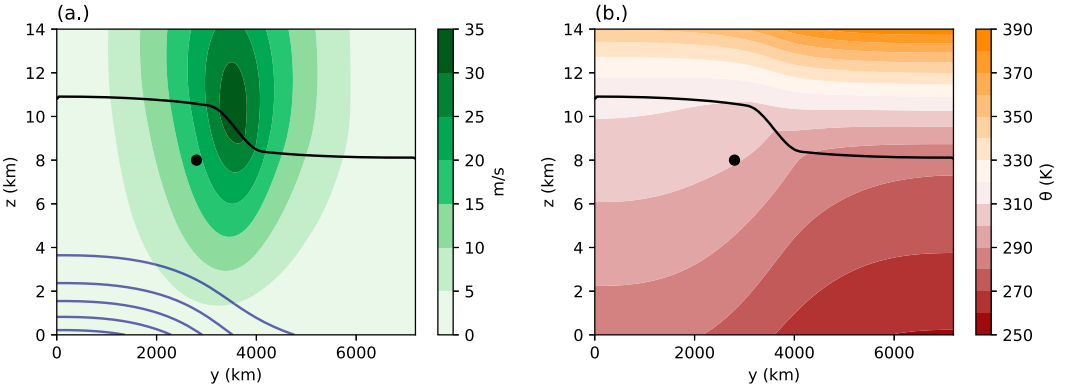

FIG. 7. North–south vertical cross section through the initial baroclinically unstable flow. (a) Jet profile $u(y, z)$ (color fill; m s^{-1}) and mixing ratio (dark blue contours at intervals of 1.5 g kg^{-1}). (b) Potential temperature (color fill; K). In both panels, the heavy black curve is the 1.5 PVU contour, indicating the tropopause, and the black point marks the (y, z) location of the center of the local PV anomaly used to seed the instability.

The coarse-mesh domain, with 12-km grid spacing, is periodic in the x direction and 9600 km wide. The domain extends 7200 km in y and is bounded by rigid sidewalls. A static 1800 km by 1800 km nest, with 4-km grid spacing, is positioned with its southwest corner at (5100 and 1884 km) as shown in Fig. 8. One-way nesting is used, and the nest is initiated at 60 h of the coarse-mesh simulation. Both domains have 100 vertical levels with the model top at approximately 20 km. Following Menchaca and Durran (2017), a Rayleigh damping layer is placed between $z = 14$ and 20 km to absorb vertically propagating gravity waves, and excessive surface wind speeds are avoided by imposing surface drag with a surface roughness length of 0.01 m. There are no surface fluxes of heat or moisture. The Kain–Fritsch cumulus parameterization (Kain 2004) is used only in the outer domain, and the two-moment NSSL microphysics scheme (Mansell et al. 2010) is used in both domains. The Coriolis parameter f was a constant 10^{-4} s^{-1}.

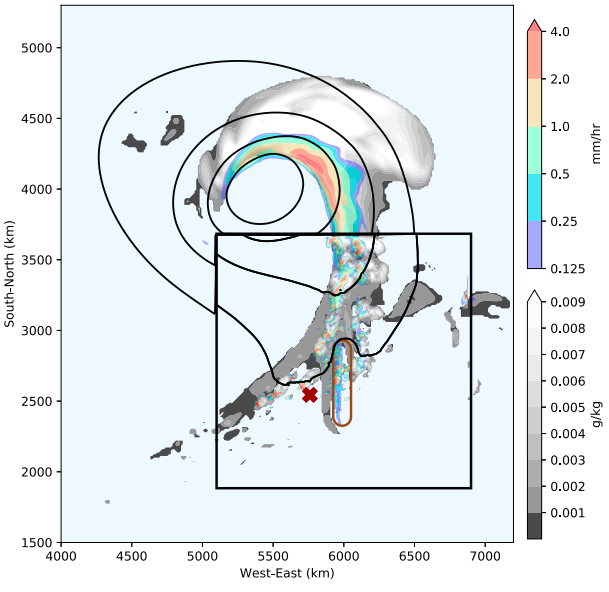

FIG. 8. Surface pressure contours (black lines every 8 hPa), precipitation (color fill; mm h^{-1}), and 6-km ice cloud mixing ratio (grayscale; g kg^{-1}) at 96 h of the Cyc+Mtn simulation. The large black square shows the location of the one-way nest, and data plotted within this square are fields from the fine mesh. The location of the ridge is indicated by the 500-m elevation contour (brown line). The red "X" denotes the location where the vertical profile was extracted to initialize the shear-flow simulation.

The terrain is an isolated ridge defined by Eq. (1) of Menchaca and Durran (2017) with $a = 60$ km and $\beta = 5$, yielding a ridge with an approximate half-width at a half-height of 60 km and a north–south to east–west aspect ratio of 5. The height of the ridge h_0 is 1 km. The center point of the ridge is $(x_0, y_0) = (6000, 2600$ km). The 500-m elevation contour for the ridge is plotted in Fig. 8.

A pair of cyclone simulations were generated with the mountain and with flat orography. Hereafter, the simulation with terrain will be referred to as the "Cyc+Mtn" simulation, and that with flat terrain will be referred to as the "Cyc-Flat" simulation. The additional, shear-flow experiment (hereafter "Shear") with horizontally uniform upstream environmental conditions is initialized with data from a sounding taken at 96 h at the location of the red "X" in Fig. 8 in the warm sector of the cyclone. This sounding is taken from the Cyc-Flat simulation to avoid any upstream influence from the ridge. The conditions at the "X" are, nevertheless, very similar in both cyclone simulations although there is slightly higher $IVT_{\perp}$ in the Cyc-Flat case. The winds were projected onto the x axis to yield the environmental profile plotted in Fig. 9.

To reduce computational costs, a smaller outer domain is used for the "Shear" simulation, with dimensions 6000 km in the east–west direction and 3000 km north–south. The inner grid has the same dimensions as in the cyclone experiments. All other numerical and microphysical parameters are the same as in the Cyc+Mtn and Cyc-Flat terrain simulations, except that the Coriolis parameter is set to zero in the Shear simulation. As in most previous idealized simulations of orographic precipitation, the winds and static-stability profiles in the Shear

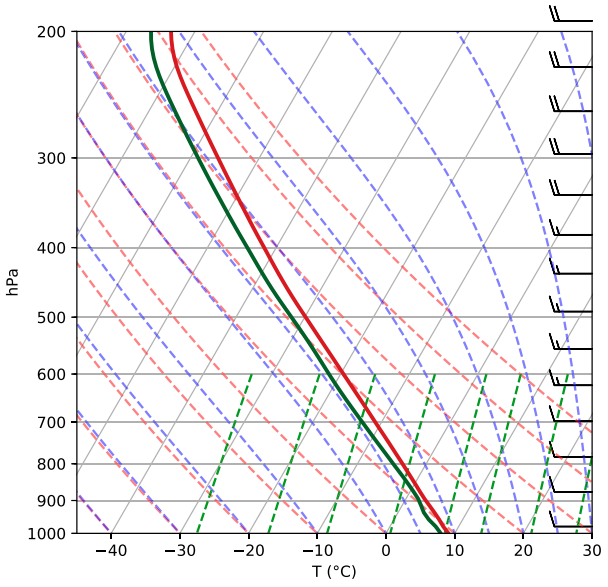

FIG. 9. Sounding profile collected from the Cyc-Flat simulation and used to initialize the shear-flow simulation: temperature (red) and dewpoint temperature (green). Wind barbs indicate the zonal wind velocity (m s^{-1}).

case are horizontally uniform. It is not possible to maintain thermal wind balance in an environment with horizontally uniform static stability and vertically varying, horizontally uniform, vertical wind shear; therefore, we set the Coriolis force to zero.[2]

One alternative to this approach, followed in Purnell and Kirshbaum (2018), is to include the action of the Coriolis force on just the perturbations from the upstream velocity profile, which implicitly assumes the upstream mass and velocity are in thermal wind balance. This approach would be expected to capture some important tendencies of the flow and precipitation to strengthen on the northern part of the mountain when $f > 0$ (Kirshbaum and Schultz 2018), but other potentially nontrivial effects, such as the advection of warmer, moister environmental air from the south by positive v velocities, would be neglected. Yet another alternative which would allow for full thermal wind balance would be to initialize the cross-mountain flow with a balanced baroclinically unstable shear flow that approximated the local conditions upstream of the mountain. Similar to the initial conditions shown in Fig. 7, this environment would have a localized, though weaker, jet but much stronger surface winds. A problem with this approach is that it would not be possible to maintain thermal wind balance during an initialization in which the flow is gradually started from rest to reduce transients generated by the presence of the mountain. In the interest of simplicity, we follow the practice of most previous idealized simulations of orographic precipitation and neglect the Coriolis force.

To reduce start-up transients, the environmental cross-mountain velocity U increases linearly from 0 to the values in Fig. 9 over a 20-h period. This also mimics the general behavior in the Cyc+Mtn case, in which the low-level winds gradually increase over a period of approximately 24 h as the low pressure center intensifies and passes to the north of the ridge. After the 20-h ramp-up, the simulation reaches a quasi-steady state. Hours 20–30 of the Shear simulation are used in the subsequent analysis.

b. *Precipitation totals*

The hourly precipitation, averaged over the windward slope of the ridge, is plotted for the Cyc+Mtn and Shear simulations as a function of simulation time in Fig. 10. Hourly precipitation totals over the same spatial region are also plotted for the Cyc-Flat case. In the Cyc+Mtn case, the passage of the warm front over the orography around simulation hour 81 is followed by a significant increase in the precipitation rate. The rain rate continues to increase and then remains high during the passage of the cold front, whose associated rainband encounters the north end of the ridge around hour 97 and finishes traversing the south end of the ridge near hour 109. In contrast, there is essentially no precipitation in the same region in the Cyc-Flat simulation until the arrival of the cold frontal rainband, again around hour 97.

In the Shear experiment, the precipitation is heaviest before the end of the 20-h ramp-up of the cross-mountain winds and then gradually diminishes to a quasi-steady 0.5 mm h^{-1}. Despite having essentially the same upstream environmental conditions as the Cyc+Mtn simulation, the precipitation in the shear-flow simulation is much lighter. From hour 21 on, it ranges from 1/2 to 1/4 of that produced during the warm-sector passage in the Cyc+Mtn case. Both within the warm sector and during the cold frontal passage, the precipitation in the Cyc+Mtn case is much heavier than that which would be produced by summing the rainfall in the Cyc-Flat and Shear simulations, so precipitation enhancement in the Cyc+Mtn case relative to the Shear case is not simply an additive contribution coming from the large-scale precipitation field.

A closer look at the evolving time and space distribution of precipitation in the Cyc+Mtn and Cyc-Flat may be obtained by dividing the 500-km-long region of the windward slope shaded blue in the inset in Fig. 10 into five 100 km × 100 km boxes. Numbering these boxes 1–5 from north to south, the hourly areal-averaged precipitation rate within each box is plotted as a function of time in Fig. 11. The 14-h north-to-south progression of the leading edge of the cold frontal precipitation is also indicated by the red line segments. Though not the focus of this study, the frontal precipitation is much heavier in the case with the ridge. The timing of the cold front passage is also just slightly different in the Mtn+Cyc and Cyc-Flat cases. The precipitation in the Cyc+Mtn case is highest in the central and north-central boxes (3 and 2) and lightest in the southern box, a nonuniform distribution

[2] Vertical variations in $\partial u/\partial z$ require vertical variations in $\partial T_v/\partial y$, which require horizontal gradients in $\partial[\partial\theta/(\partial z)\partial y]$ that (for realistic moisture distributions) violate the assumption of uniform static stability throughout horizontal layers. (Here, T_v is the virtual temperature.)

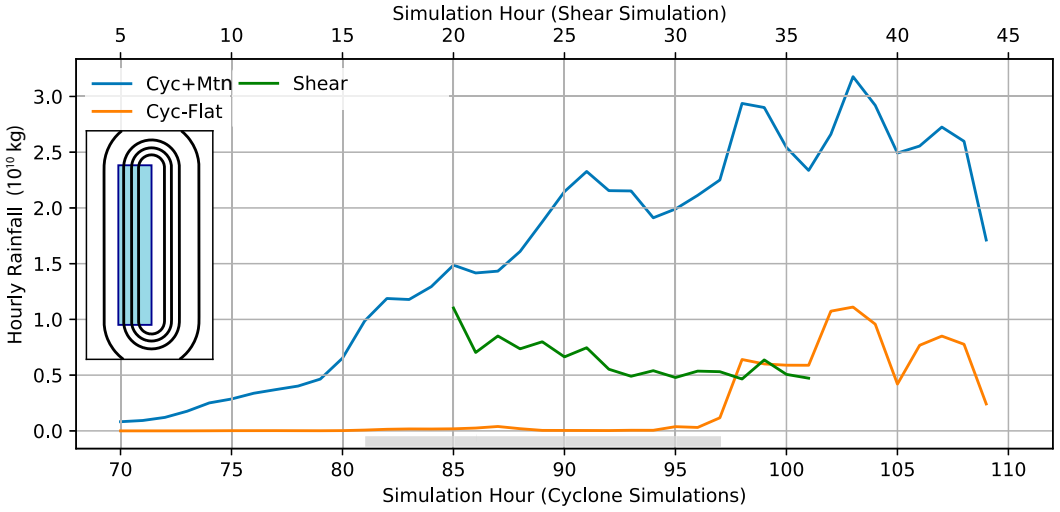

FIG. 10. The mean hourly precipitation integrated over the region containing the windward slope of the ridge (blue shaded area on the inset) plotted as a function of simulation time. Cyc+Mtn case: blue, Cyc-Flat case: orange, and Shear case: green. Gray shading shows the period when the warm sector lies above the location of the windward slope.

produced by the complex evolving large-scale flow and the influence of the Coriolis force.

Given the complexity of the large-scale flow, a thorough investigation of the sources of temporal and along-ridge variability in the precipitation in the Mtn+Cyc simulation is beyond the scope of this study. For comparison with the unidirectional Shear simulation, we wish to focus on a period before the front starts to interact with the mountain when the flow is quasi-steady and quasi-unidirectional. As illustrated by the purple vertical lines in Fig. 11, the period from 85 to 95 h provides such an opportunity for the section of the mountain covered by boxes 2 and 3. The spatial distribution of the 10-h mean precipitation over this period is shown in Fig. 12. Throughout 85–95 h, most of the precipitation in the Cyc+Mtn case falls over the northern 60% of the ridge, where it begins near the upstream foot of the ridge and extends episodically past the crest. The peak accumulation occurs between elevations of 600 and 800 m. In contrast, to the mean over hours 20–30 in the Shear case, nearly all of the precipitation falls between elevations of 800 m and the ridge crest at 1000 m. The region of intense rainfall, with 10-h accumulations exceeding 1 cm, is much greater in the Cyc+Mtn case than in the Shear case.

c. $IVT_{\perp}$ and rainfall rate

How does the relationship between $IVT_{\perp}$ and rainfall rate for the Cyc+Mtn and Shear simulations compare to the previously discussed observed and idealized simulation results? Data for hours 84, 90, and 96 from the Cyc+Mtn case is shown by the purple dots in Fig. 6. These points plot $IVT_{\perp}$ evaluated at the start of a 1-h period at the foot of the terrain (x = 780 km and y = 700 km) against the 1-h precipitation rate averaged over the windward slope and the 60-km north–south transect $700 \le y \le 760$ km indicated by the red dashed box in Fig. 12. The $IVT_{\perp}$ is computed at the southern end of the transect because the low-level velocity is directed from the southwest.

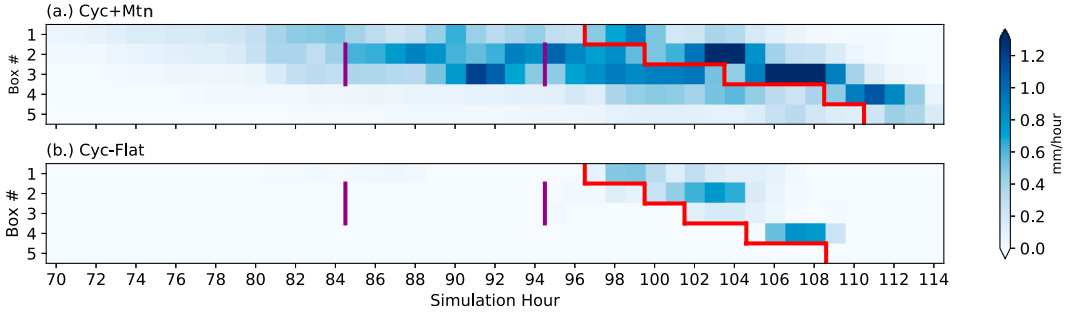

FIG. 11. Hourly and spatially averaged precipitation rates (mm h^{-1}) in each of five boxes equally dividing the blue shaded upslope region in Fig. 10 in a north-to-south direction: (a) Mtn+Cyc and (b) Cyc-Flat simulation. Purple vertical lines drawn for boxes 2 and 3 delimit a 10-h warm-sector period beginning at 85 and ending a 95 h. Tick marks are centered on each hour. Red line segments mark the approximate arrival of the cold front precipitation in each box.

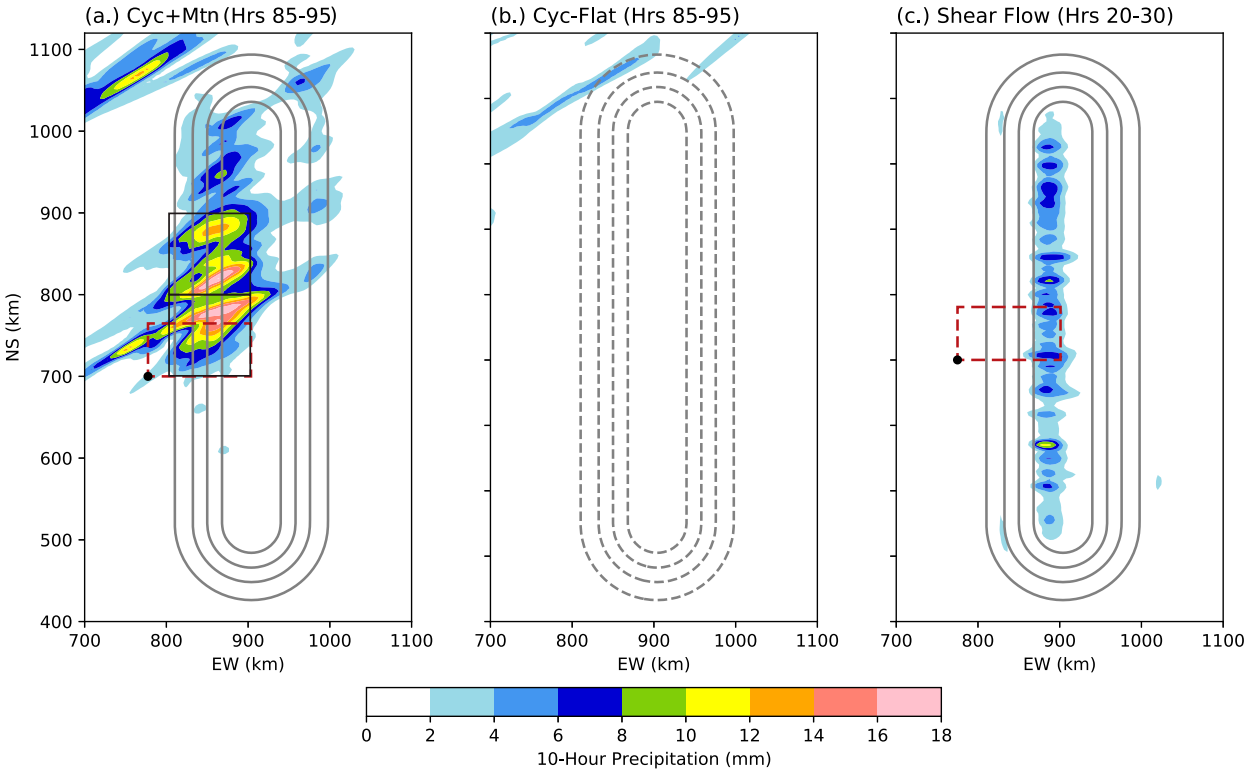

FIG. 12. 10-h precipitation totals (mm) over (a),(b) 85–95 h from the Cyc+Mtn and the Cyc-Flat simulations, respectively, and (c) 20–30 h from the shear-flow case. Terrain contours are every 200 m (black lines); x and y coordinates are relative to the origin of the nested mesh (at its SW corner). Red dashed boxes show the portion of the ridge used in the computation of the Cyc+Mtn and Shear precipitation in Fig. 6 (purple symbols). The $IVT_{\perp}$ for those calculations is evaluated in the column above the black dot on the upstream corner of the box. Thin black squares in (a) show the location of boxes 2 and 3.

The width and location of the windward-slope transect used for comparison with observations are necessarily arbitrary. The observations from the Olympics are spread over a swath <20 km wide (Fig. 1). Other observational studies involve single gauges. Data from previous numerical simulations were estimated over swaths ranging from a single line (Kirshbaum and Schultz 2018) to an infinitely wide region in the 2D simulations of Colle (2004). Motivated by the OLYMPEX sites, our swath is relatively narrow but is expanded to a width of 15 grid cells to avoid sensitivities to poorly resolved circulations. The swath is located at the southern end of boxes 2 and 3, which, as discussed in connection with Fig. 11, are our focus during warm-sector passage. The distribution of the 10-h precipitation shown in Fig. 12 suggests this choice of location within boxes 2 and 3 minimizes the simulated precipitation rate—in contrast to the upper-bound precipitation estimates from previous simulations forced by unidirectional shear flows plotted in Fig. 6.

Over the period between 84 and 96 h, the $IVT_{\perp}$ and rainfall rates in the Cyc+Mtn simulation increase as the cold front advances toward the mountain, yet for each time, the points lie close to the best-fit line for the OLYMPEX cases. These $IVT_{\perp}$ and precipitation totals are modest compared to the OLMPEX events because the idealized cyclone is designed to represent a typical midlatitude cyclone, not the more extreme OLMPEX cases, but the key result is that when the circulation associated with the cyclone is included in the simulation, we obtain the observed relation between $IVT_{\perp}$ and orographic rainfall.

In the Shear case, the mean windward-slope precipitation rate and IVT are retrieved from the same geographic location used in the Cyc+Mtn simulation, but the values are averaged over the quasi-steady period 20–30 h and plotted as the purple triangle in Fig. 6. The same $IVT_{\perp}$ values generate far less orographic precipitation in the Shear simulation; instead, the relation between $IVT_{\perp}$ and precipitation is more characteristic of previously published idealized simulations forced by unidirectional flow. In a companion paper (Tierney and Durran 2024), we analyze the reason for the difference in the precipitation between the Cyc+Mtn and Shear cases.

d. Embedded convection

The precipitation in both the Cyc+Mtn and Shear cases is dominated by embedded convective cells though their structures differ between the simulations. The liquid water concentrations in the orographic clouds are contrasted in Fig. 13 which are contoured for 200-km north–south (N-S) sections of the orography. The cells in the Cyc+Mtn case are deeper and more randomly distributed; some develop upstream of the terrain, while others first appear over the windward slope

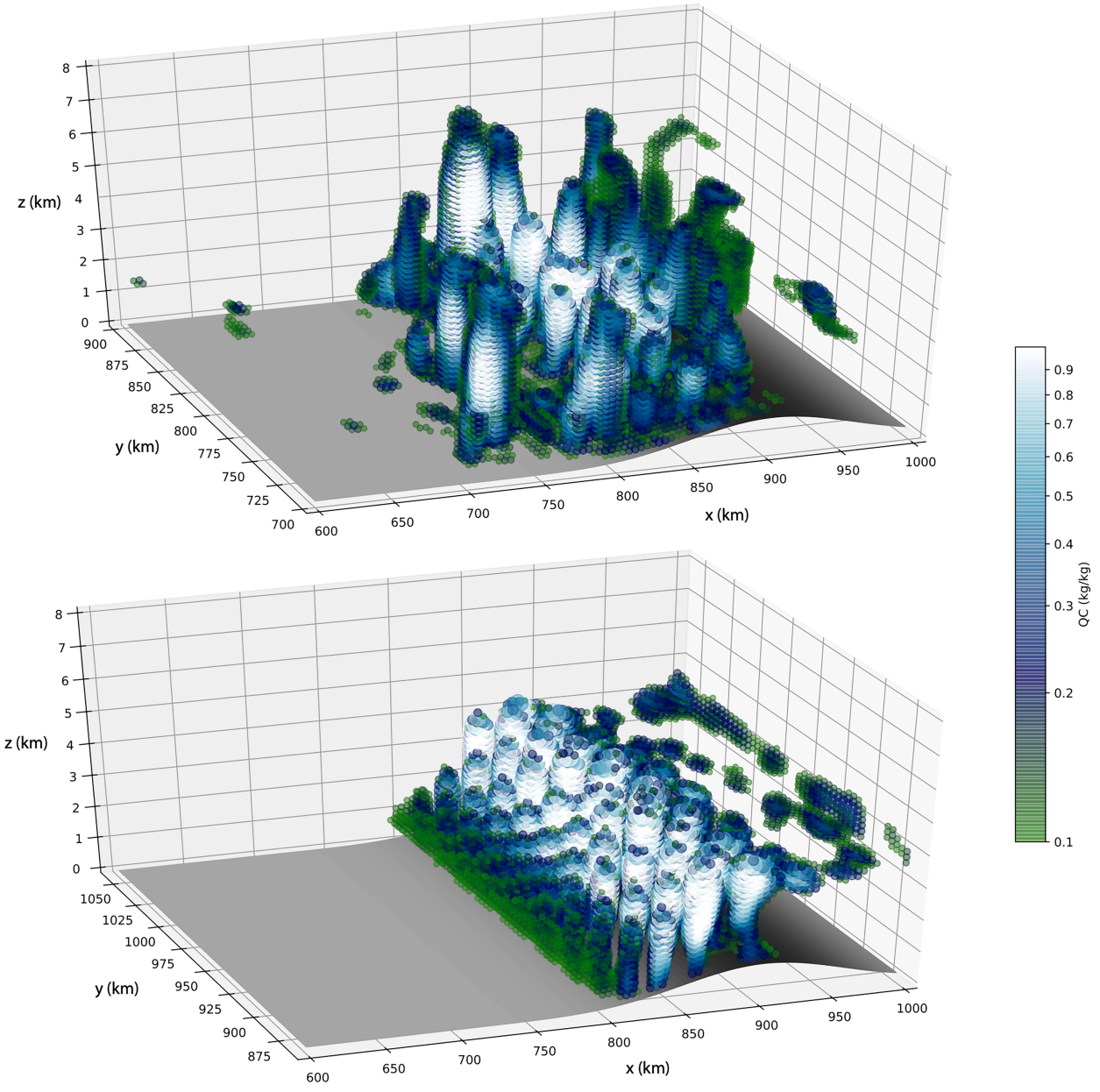

FIG. 13. Cloud liquid water content q_c within a cross-ridge swath from $y = 700$ to 900 km. (top) Cyc+Mtn case at 88 h and (bottom) Shear simulation at 25 h. The mixing ratio is indicated both by the color scale and by increasing the diameter of each point in proportion to the increase in concentration.

(Fig. 13, top). In contrast, the convective cells are shallower in the Shear simulation, and they do not develop until the flow starts to ascend the windward slope. The cells are also more tightly and regularly packed in the Shear case. The quasi-regularity in the Shear case is likely due to the lack of modest-amplitude random perturbations in the upstream flow and the 4-km "convection-permitting" resolution, which reduces the growth rate of fine-scale convective features. Because of the 4-km grid spacing, the width of the convective cores in these cells is unrealistically large. Nevertheless, as illustrated in Fig. 14, the vertical extent and structure of the cells in the Cyc+Mtn simulation are representative of some periods of embedded convection observed by the NCAR/Earth Observing Laboratory (EOL) S-POL radar during OLYMPEX.

5. Conclusions

Observational studies have established that cold-season orographic precipitation totals are dominated by events involving the passage of synoptic systems. Observations have also demonstrated a strong correlation between integrated vapor transport and orographic precipitation. These results fit

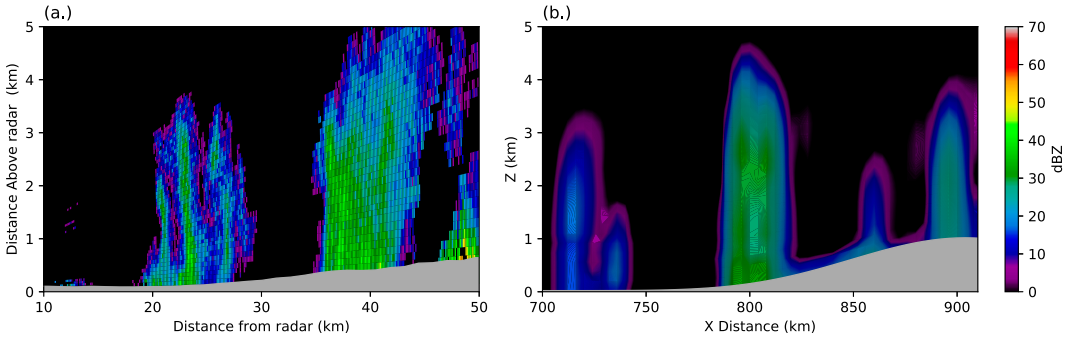

FIG. 14. (a) RHI radar reflectivity scan from Taholah at 0255 UTC 13 Dec 2015 oriented up the Quinault River valley. The mean terrain height across a 10-km-wide segment perpendicular to the scan is shown in gray. (b) Synthetic reflectivity from the Cyc+Mtn simulation at 85 h along $y = 800$ km. Note the difference in the horizontal scale.

easily into the theoretical context of precipitation forced by ascent as moist airflow in the warm sector of midlatitude cyclones encounters an orographic barrier. The flow in the warm sector is often nearly unidirectional with height and cross-flow horizontal coordinate, so orographic precipitation in these cases might appear to be well suited for analysis using simulations in which a unidirectional flow impinges on a mountain. Indeed, many previous process studies involve such simulations.

Yet surprisingly, the $IVT_{\perp}$ in process studies forced by horizontal shear flows yields far less precipitation than that which would be suggested by the observational analysis presented in this paper. For the observational dataset, we relied primarily on rain gauges and soundings deployed during the OLMPEX project. Interestingly, the least squares best-fit line for precipitation as a function of $IVT_{\perp}$ computed from the OLMPEX data is almost identical to that obtained previously in a study of orographic precipitation over the much lower coastal ridges of Sonoma County in Northern California (Kingsmill et al. 2016).

We surveyed previous idealized process studies forced by horizontal shear flows, including 2D and 3D simulations over long ridges, and 3D simulations over the actual orography of the Olympic Mountains. Some of these studies use mesoscale numerical models that are known to produce roughly correct precipitation totals in full case studies or operational forecasts. Nevertheless, as apparent in Fig. 6, in all the process studies the precipitation rates produced by a given upstream $IVT_{\perp}$ are much lower than in the observations.

As a first step toward understanding the deficiency in process studies with simple horizontally uniform atmospheric forcing, we simulated an idealized midlatitude cyclone growing in a moist baroclinically unstable background flow in an *f*-plane channel. The low center in this Cyc+Mtn simulation passed north of an elongated north–south ridge and produced substantial orographic precipitation as its warm-sector flow interacted with the ridge. Our prototypical midlatitude cyclone produced lower precipitation rates than most of the more extreme OLMPEX cases, but the relation between $IVT_{\perp}$ and precipitation rate, computed at three different times as the cyclone approached the ridge, closely followed that obtained from observational data. In contrast, a second Shear simulation, forced by horizontally homogeneous vertically sheared flow matching the environmental conditions at a point upstream of the mountain, produced far less precipitation than the full Cyc+Mtn simulation. The relation between $IVT_{\perp}$ and precipitation rate in the Shear simulation was comparable to that in many previous idealized process model simulations. In a companion paper (Tierney and Durran 2024), we diagnose the factors responsible for the difference in precipitation rates between the Cyc+Mtn and Shear simulations, which we believe also account for differences in the $IVT_{\perp}$–precipitation relationship revealed in this study between observations and idealized simulations forced by unidirectional horizontal large-scale flows.

Acknowledgments. The paper was significantly improved by comments from anonymous reviewers. This research was supported by NSF Grants AGS-1545927 and AGS-1929466. High-performance computing support from Cheyenne (https://doi.org/10.5065/D6RX99HX) was provided by the NCAR's Computational and Information Systems Laboratory, sponsored by the National Science Foundation. This work also relied on computational resources at the Extreme Science and Engineering Discovery Environment (XSEDE) which is supported by the National Science Foundation Grant ACI-1548562.

Data availability statement. The sounding data from the OLYMPEX experiment are archived at https://doi.org/10.26023/84TC-F4DR-90E. Range gauge and other OLMPEX data are archived at http://dx.doi.org/10.5067/GPMGV/OLYMPEX/DATA101. The output data from our simulations are too large to archive but may be regenerated using the community WRF Model. The technique for initializing idealized *f*-plane baroclinically unstable flows is thoroughly discussed in Lloveras and Durran (2024). The Python code for generating such initial conditions and the instructions for evolving them in WRF are publicly available at https://github.com/lloverasdan/init-bwave. The WRF Model is available at https://www.mmm.ucar.edu/models/wrf.

APPENDIX

Data and Calculations from Prior Publications

Colle (2004) presents seventeen 2D numerical simulations with different upstream initial sounding profiles and terrain geometries. IVT values were not directly reported; however, the moist static stability, freezing level, surface pressure, relative humidity, and wind profiles were available for each case, and the IVT for the complete sounding profile was computed from these quantities. Using 6-h precipitation totals that were plotted as a function of the cross-terrain coordinate (e.g., his Fig. 2), we took the highest precipitation value along the cross-terrain transect to compute an hourly rain rate. This procedure clearly yields a relatively crude upper bound on the average windward-slope precipitation rate, yet this is adequate for our comparison purposes because even this upper bound is far lower than the precipitation rates that would be expected for a given IVT based on observations (see Fig. 6).

The characteristics of the upstream flow and mountain geometry for this set of experiments are detailed in Table A1. The experiments we consider have mountain half-widths at half-height of 50 km and upstream moist static stabilities of 0.01 s^{-1}. We do not include the "wide mountain (WM)" cases with heights exceeding 1500 m because our observed cases all have an orography of 1500 m or less and because blocking can become an issue in 2D simulations with high orography. We also did not include "WM" or "FL500" simulations with 30 m s^{-1} wind speeds because these simulations had very high IVT values and would lie off of the horizontal axis of Fig. 6.

Cannon et al. (2012) conducted two groups of numerical experiments, one that permitted convection and one in which convection was numerically suppressed. We used only the data from the convection permitting cases, so as not to underestimate our precipitation totals. All five upstream sounding profiles are used in our analysis, with IVT values ranging from 146 to 325 kg m^{-1} s^{-1}. The only reported precipitation metric was the cross-ridge precipitation rate, integrated from far upstream of the terrain to a point downstream of the crest. To avoid underestimating the rainfall rate, we calculated an average upslope precipitation rate by assuming all this precipitation fell in the region between the crest and a location $2a$ upstream, where a is the half-width of the Gaussian cross-mountain profile used in their simulations. We used data from the experiments with terrain heights of 1 km and half-widths of $a = 30$ km and $a = 60$ km and plotted the average of these two values for each IVT. This averaging procedure is motivated by our estimate of an equivalent value for a for the Olympics of 45 km.

Last, the upslope precipitation in Siler and Durran (2015) was determined by dividing the cross-ridge-integrated precipitation rate reported in their Fig. 8 by $2a$, where the mountain half-width a is 25 km. IVT values are calculated from the upstream U, N, relative humidity, and surface temperature values for the 3D ridge, linear-shear experiments listed in Siler and Durran (2015, section 2c).

TABLE A1. Summary of experiments used from Colle (2004).

Experiment	Freezing level (hPa)	Mtn height (km)	Cross-mtn velocity (m s^{-1})
FL1000	1000	1.5	5, 10, … 30
WM	750	0.5, 1.0, 1.5	10, 20
FL500	500	1.5	10, 20

REFERENCES

Barrett, B. S., R. Garreaud, and M. Falvey, 2009: Effect of the Andes cordillera on precipitation from a midlatitude cold front. *Mon. Wea. Rev.*, **137**, 3092–3109, https://doi.org/10.1175/2009MWR2881.1.

Cannon, D. J., D. J. Kirshbaum, and S. L. Gray, 2012: Under what conditions does embedded convection enhance orographic precipitation? *Quart. J. Roy. Meteor. Soc.*, **138**, 391–406, https://doi.org/10.1002/qj.926.

Colle, B. A., 2004: Sensitivity of orographic precipitation to changing ambient conditions and terrain geometries: An idealized modeling perspective. *J. Atmos. Sci.*, **61**, 588–606, https://doi.org/10.1175/1520-0469(2004)061<0588:SOOPTC>2.0.CO;2.

Doyle, J. D., and N. A. Bond, 2001: Research aircraft observations and numerical simulations of a warm front approaching Vancouver Island. *Mon. Wea. Rev.*, **129**, 978–998, https://doi.org/10.1175/1520-0493(2001)129<0978:RAOANS>2.0.CO;2.

Field, P. R., and R. Wood, 2007: Precipitation and cloud structure in midlatitude cyclones. *J. Climate*, **20**, 233–254, https://doi.org/10.1175/JCLI3998.1.

Fleming, E. L., S. Chandra, J. J. Barnett, and M. Corney, 1990: Zonal mean temperature, pressure, zonal wind and geopotential height as functions of latitude. *Adv. Space Res.*, **10**, 11–59, https://doi.org/10.1016/0273-1177(90)90386-E.

Houze, R. A., Jr., and Coauthors, 2017: The Olympic Mountains Experiment (OLYMPEX). *Bull. Amer. Meteor. Soc.*, **98**, 2167–2188, https://doi.org/10.1175/BAMS-D-16-0182.1.

Hughes, M., A. Hall, and R. G. Fovell, 2009: Blocking in areas of complex topography, and its influence on rainfall distributions. *J. Atmos. Sci.*, **66**, 508–518, https://doi.org/10.1175/2008JAS2689.1.

Kain, J. S., 2004: The Kain–Fritsch convective parameterization: An update. *J. Appl. Meteor.*, **43**, 170–181, https://doi.org/10.1175/1520-0450(2004)043<0170:TKCPAU>2.0.CO;2.

Kingsmill, D. E., P. J. Neiman, and A. B. White, 2016: Microphysics regime impacts on the relationship between orographic rain and orographic forcing in the coastal mountains of northern California. *J. Hydrometeor.*, **17**, 2905–2922, https://doi.org/10.1175/JHM-D-16-0103.1.

Kirshbaum, D. J., and D. M. Schultz, 2018: Convective cloud bands downwind of mesoscale mountain ridges. *J. Atmos. Sci.*, **75**, 4265–4286, https://doi.org/10.1175/JAS-D-18-0211.1.

Lloveras, D. J., and D. R. Durran, 2024: Improving the representation of moisture and convective instability in baroclinic-wave channel simulations. *Mon. Wea. Rev.*, **152**, 1469–1486, https://doi.org/10.1175/MWR-D-23-0210.1, in press.

Lundquist, J. D., J. R. Minder, P. J. Neiman, and E. Sukovich, 2010: Relationships between barrier jet heights, orographic precipitation gradients, and streamflow in the northern Sierra Nevada. *J. Hydrometeor.*, **11**, 1141–1156, https://doi.org/10.1175/2010JHM1264.1.

Mansell, E. R., C. L. Ziegler, and E. C. Bruning, 2010: Simulated electrification of a small thunderstorm with two-moment bulk

microphysics. *J. Atmos. Sci.*, **67**, 171–194, https://doi.org/10.1175/2009JAS2965.1.

Marshall, J., and R. A. Plumb, 2012: *Atmosphere, Ocean, and Climate Dynamics: An Introductory Text*. Elsevier, 344 pp.

McMurdie, L. A., A. K. Rowe, R. A. Houze Jr., S. R. Brodzik, J. P. Zagrodnik, and T. M. Schuldt, 2018: Terrain-enhanced precipitation processes above the melting layer: Results from OLYMPEX. *J. Geophys. Res. Atmos.*, **123**, 12 194–12 209, https://doi.org/10.1029/2018JD029161.

Menchaca, M. Q., and D. R. Durran, 2017: Mountain waves, downslope winds, and low-level blocking forced by a midlatitude cyclone encountering an isolated ridge. *J. Atmos. Sci.*, **74**, 617–639, https://doi.org/10.1175/JAS-D-16-0092.1.

Michaelis, A. C., A. C. Martin, M. A. Fish, C. W. Hecht, and F. M. Ralph, 2021: Modulation of atmospheric rivers by mesoscale frontal waves and latent heating: Comparison of two U.S. west coast events. *Mon. Wea. Rev.*, **149**, 2755–2776, https://doi.org/10.1175/MWR-D-20-0364.1.

Minder, J. R., D. R. Durran, G. H. Roe, and A. M. Anders, 2008: The climatology of small-scale orographic precipitation over the Olympic Mountains: Patterns and processes. *Quart. J. Roy. Meteor. Soc.*, **134**, 817–839, https://doi.org/10.1002/qj.258.

——, ——, and ——, 2011: Mesoscale controls on the mountain-side snow line. *J. Atmos. Sci.*, **68**, 2107–2127, https://doi.org/10.1175/JAS-D-10-05006.1.

Neiman, P. J., F. M. Ralph, A. B. White, D. E. Kingsmill, and P. O. G. Persson, 2002: The statistical relationship between upslope flow and rainfall in California's coastal mountains: Observations during CALJET. *Mon. Wea. Rev.*, **130**, 1468–1492, https://doi.org/10.1175/1520-0493(2002)130<1468:TSRBUF>2.0.CO;2.

——, A. B. White, F. M. Ralph, D. J. Gottas, and S. I. Gutman, 2009: A water vapour flux tool for precipitation forecasting. *Proc. Inst. Civil Eng. Water Manage.*, **162**, 83–94, https://doi.org/10.1680/wama.2009.162.2.83.

Picard, L., and C. Mass, 2017: The sensitivity of orographic precipitation to flow direction: An idealized modeling approach. *J. Hydrometeor.*, **18**, 1673–1688, https://doi.org/10.1175/JHM-D-16-0209.1.

Purnell, D. J., and D. J. Kirshbaum, 2018: Synoptic control over orographic precipitation distributions during the Olympics Mountains Experiment (OLYMPEX). *Mon. Wea. Rev.*, **146**, 1023–1044, https://doi.org/10.1175/MWR-D-17-0267.1.

Rutz, J. J., W. J. Steenburgh, and F. M. Ralph, 2014: Climatological characteristics of atmospheric rivers and their inland penetration over the western United States. *Mon. Wea. Rev.*, **142**, 905–921, https://doi.org/10.1175/MWR-D-13-00168.1.

Siler, N., and D. Durran, 2015: Assessing the impact of the tropopause on mountain waves and orographic precipitation using linear theory and numerical simulations. *J. Atmos. Sci.*, **72**, 803–820, https://doi.org/10.1175/JAS-D-14-0200.1.

Skamarock, W. C., and J. B. Klemp, 2008: A time-split nonhydrostatic atmospheric model for research and NWP applications. *J. Comput. Phys.*, **227**, 3465–3485, https://doi.org/10.1016/j.jcp.2007.01.037.

Tierney, L., and D. Durran, 2024: Underestimates of orographic precipitation in idealized simulations. Part II: Underlying causes. *J. Atmos. Sci.*, **81**, 1435–1447, https://doi.org/10.1175/JAS-D-23-0176.1.

Viale, M., and M. N. Nuñez, 2011: Climatology of winter orographic precipitation over the subtropical central Andes and associated synoptic and regional characteristics. *J. Hydrometeor.*, **12**, 481–507, https://doi.org/10.1175/2010JHM1284.1.

Wilcox, L. J., B. J. Hoskins, and K. P. Shine, 2011: A global blended tropopause based on era data. Part I: Climatology. *Quart. J. Roy. Meteor. Soc.*, **138**, 561–575, https://doi.org/10.1002/qj.951.

Zagrodnik, J. P., L. A. McMurdie, R. A. Houze Jr., and S. Tanelli, 2019: Vertical structure and microphysical characteristics of frontal systems passing over a three-dimensional coastal mountain range. *J. Atmos. Sci.*, **76**, 1521–1546, https://doi.org/10.1175/JAS-D-18-0279.1.

——, L. McMurdie, and R. Conrick, 2021: Microphysical enhancement processes within stratiform precipitation on the barrier and sub-barrier scale of the Olympic Mountains. *Mon. Wea. Rev.*, **149**, 503–520, https://doi.org/10.1175/MWR-D-20-0164.1.